Electronic Supplementary Information (ESI)

Anti-freezing flexible aqueous Zn-MnO_2 battery working at –35 °C enabled by borax-crosslinked polyvinyl alcohol/glycerol gel electrolyte

Minfeng Chen,[a] Weijun Zhou,[a] Anran Wang,[a] Aixiang Huang,[a] Jizhang Chen,*[a] Junling Xu[b] and Ching-Ping Wong*[bc]

[a] *College of Materials Science and Engineering, Nanjing Forestry University, Nanjing 210037, China*

[b] *Department of Electronic Engineering, The Chinese University of Hong Kong, Hong Kong, China*

[c] *School of Materials Science and Engineering, Georgia Institute of Technology, Atlanta, United States*

E-mail addresses: chenjizhang@njfu.edu.cn (J. Chen), cp.wong@mse.gatech.edu (C.-P. Wong).

Experimental details

Preparation of the rGO/MnO_2 nanocomposite

Graphene oxide (GO) was synthesized according to our previous report.[1] The obtained GO was calcined in a tubular furnace at 800 ℃ in argon atmosphere for 1 h to obtain reduced GO (rGO). Then, 0.1 g rGO was dispersed in 150 mL deionized water with the assistance of ultrasonication. After that, 12 mmol of $Mn(CH_3COO)_2 \cdot 4H_2O$ was added into the above dispersion under stirring. The obtained dispersion was added dropwise into 80 mL aqueous solution containing 8 mmol $KMnO_4$, followed by vigorous stirring for 1 h. Subsequently, the dispersion was transferred to a Teflon-lined autoclave and kept at 130 ℃ for 12 h. After hydrothermal treatment, the dark brown precipitate (*i.e.*, rGO/MnO_2) was washed with deionized water and then freeze dried.

Measurements of ionic conductivity

The ionic conductivity (σ) of gel electrolytes was estimated using electrochemical impedance spectroscopy (EIS) measurements over a frequency from 100 kHz to 0.01 Hz. The EIS measurements were conducted by sandwiching the gel electrolytes between two stainless steel sheets. As for the liquid electrolyte, a Whatman GF/A filter paper filled with 2 M $ZnSO_4$/0.2 M $MnSO_4$ aqueous solution was used for EIS measurements under the same condition. According to the obtained Nyquist plots, σ (mS cm^{-1}) could be calculated as:

$$\sigma = \frac{100d}{RA} \qquad (1)$$

where R (Ω) represents the bulk resistance determined from the intercept with real axis, and d (mm) and A (cm^2) are the thickness and area of the gel electrolytes or separator, respectively.

Supplementary figures

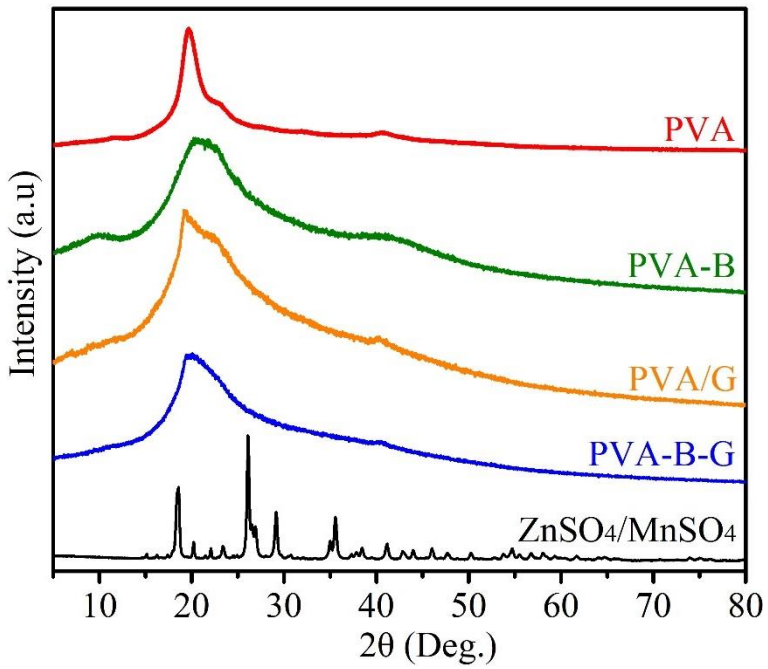

Fig. S1 XRD patterns of freeze-dried pure PVA (raw material), PVA-B, PVA/G, PVA-B-G, and $ZnSO_4/MnSO_4$. Before XRD measurements, the PVA and $ZnSO_4/MnSO_4$ were dissolved in water and then freeze dried.

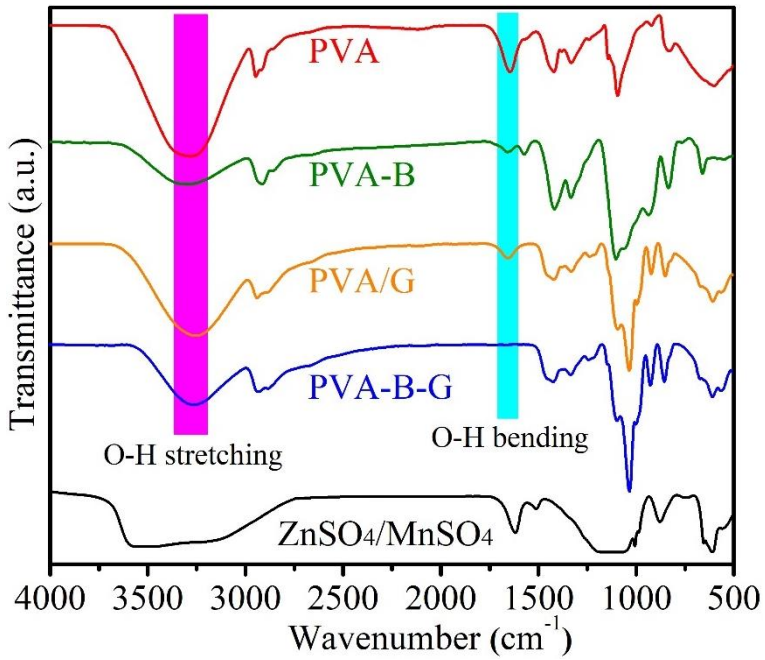

Fig. S2 FTIR spectra of freeze-dried pure PVA (raw material), PVA-B, PVA/G, PVA-B-G, and $ZnSO_4/MnSO_4$. Before FTIR measurements, the PVA and $ZnSO_4/MnSO_4$ were dissolved in water and then freeze dried.

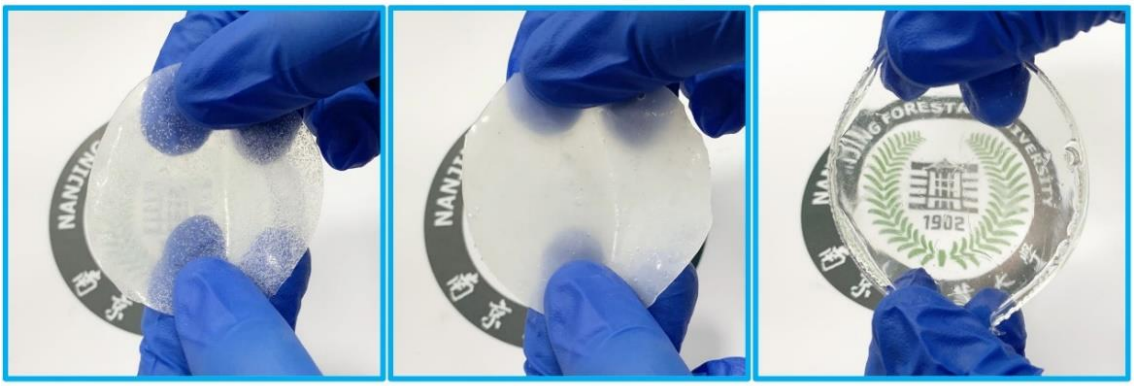

Fig. S3 Photographs of PVA-B and PVA/G in comparison with PVA-B-G.

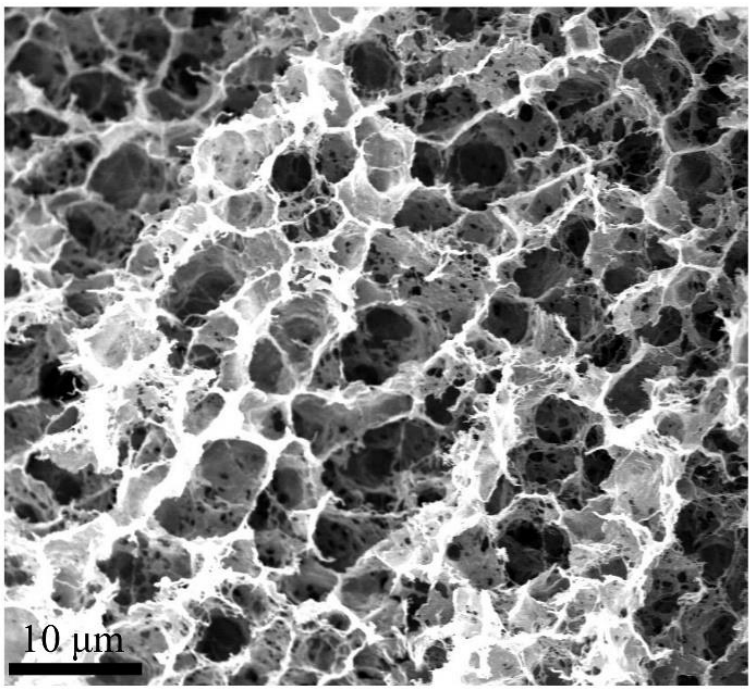

Fig. S4 SEM image of the freeze-dried PVA-B-G.

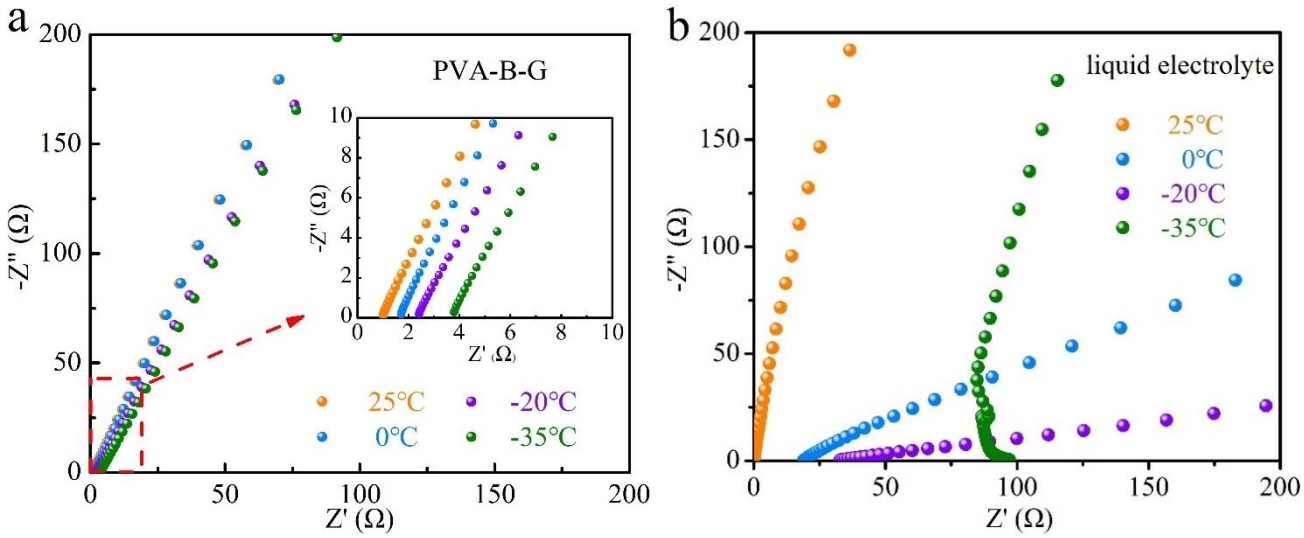

Fig. S5 Nyquist plots of (a) PVA-B-G and (b) liquid electrolyte, measured in a stainless steel// electrolyte// stainless steel configuration.

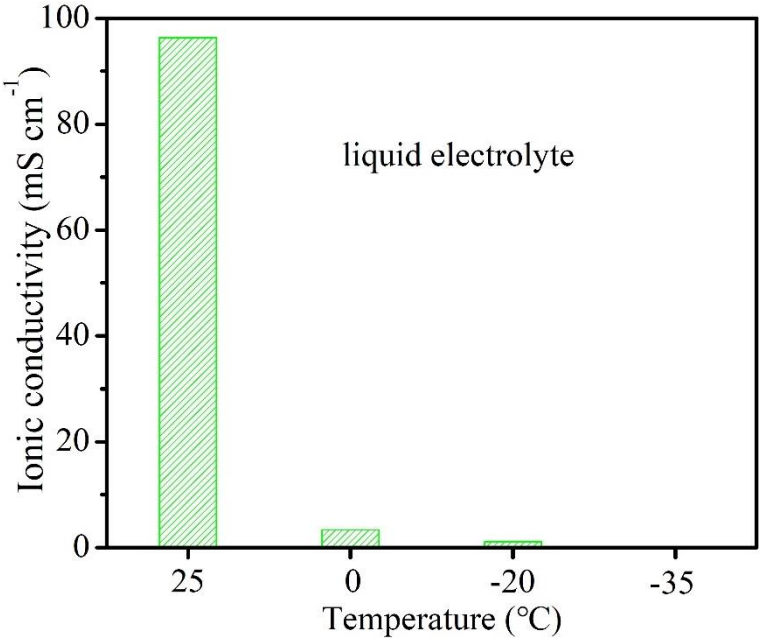

Fig. S6 The ionic conductivity of liquid electrolyte as a function of temperature.

Table S1 The ionic conductivity comparison of PVA-B-G in this work with recently reported gel electrolytes for AZIBs or AZHSs. Unless specified, the ionic conductivity data from the literature was probably collected at room temperature (R.T.).

Gel electrolyte	Ionic conductivity (mS cm^{-1})	Reference
PVA-B-G	29.6 at 25 ºC 15.9 at −20 ºC 10.1 at −35 ºC	This work
EG-waPUA/PAM	16.8 at 20 °C 14.6 at −20 °C	2
xanthan gum	16.5 at R.T. 2.5 at −8 ºC	3
PAM/concentrated electrolyte	9.1 at 25 °C 1.5 at −15 °C	4
HCZLE-PAM	5.03 at 20 °C 3.17 at −15 °C	5
PVA	12.6	6
PAM	17.3	7
PVA-COOH	25.8	8
PAM/gelatin	17.6	9
starch/PAM	26.5	10
PAM/nanofibrillated cellulose	22.8	11
PAM/concentrated electrolyte	4.5	12
PAA	21.7	13
gelatin	6.1	14
guar gum	10.7	15
PEO/PPO	6.33	16

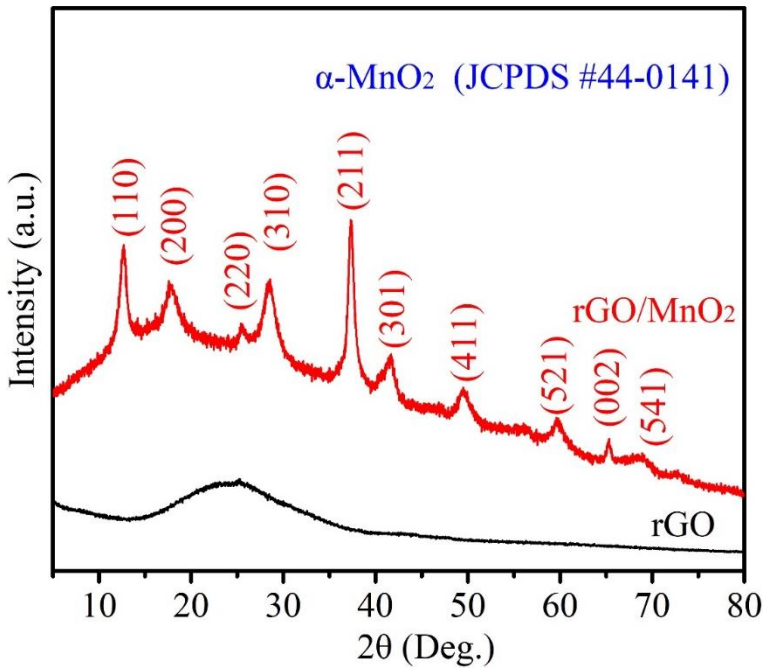

Fig. S7 XRD patterns of rGO/MnO_2 nanocomposite and rGO.

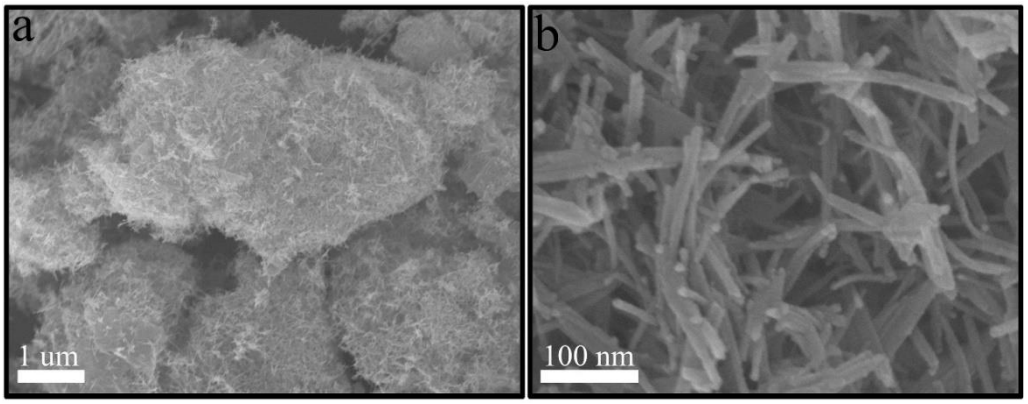

Fig. S8 (a, b) SEM images of the rGO/MnO_2 nanocomposite.

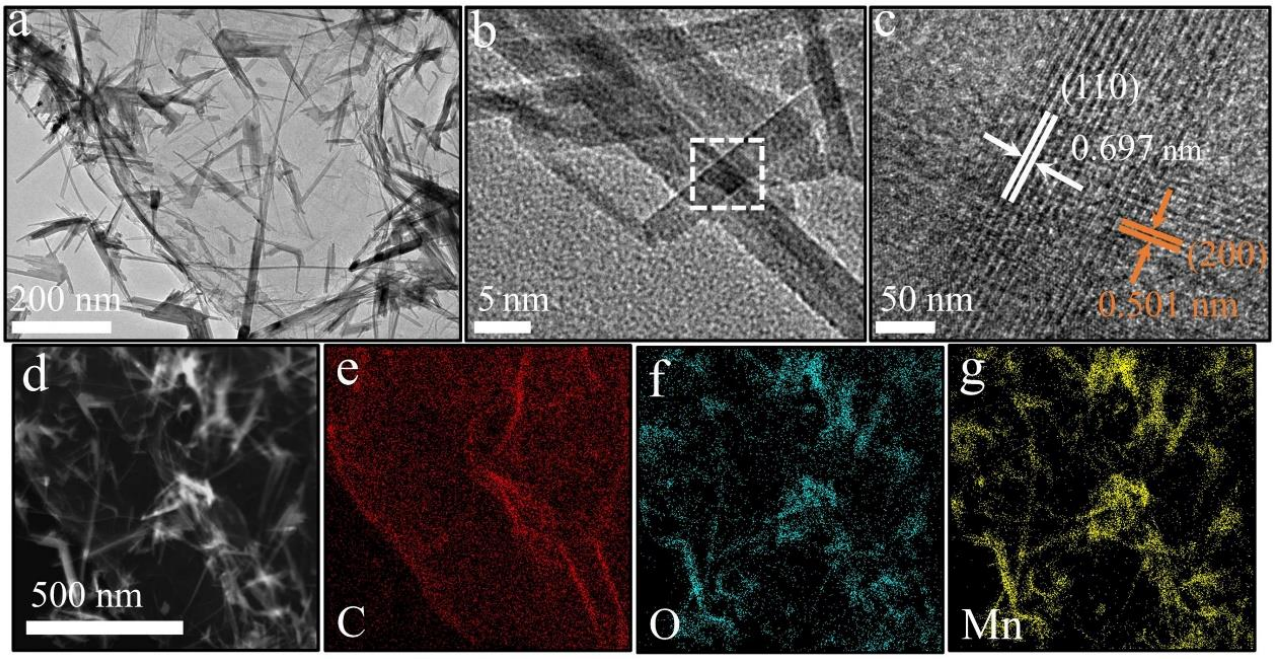

Fig. S9 (a, b) TEM images, (c) HRTEM image, (d) STEM image, and (e, f, g) EDX mapping images of the rGO/MnO_2 nanocomposite.

In Fig. S9c, the HRTEM image exhibits lattice distances of 0.697 and 0.501 nm, which are assigned to the (110) and (200) planes of α-MnO_2, respectively.

Fig. S10 Photograph of measuring the thickness of PVA-B-G battery with a micrometer caliper.

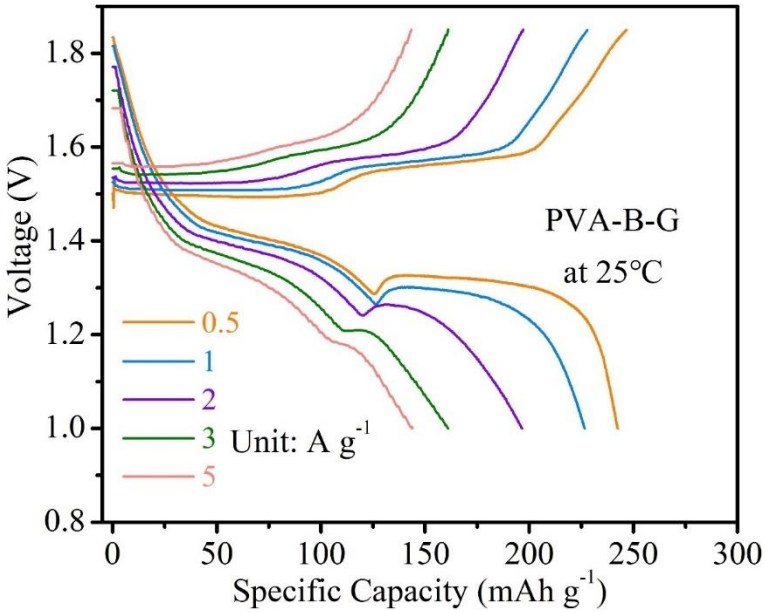

Fig. S11 GCD curves of the PVA-B-G battery at different current densities at 25 ºC.

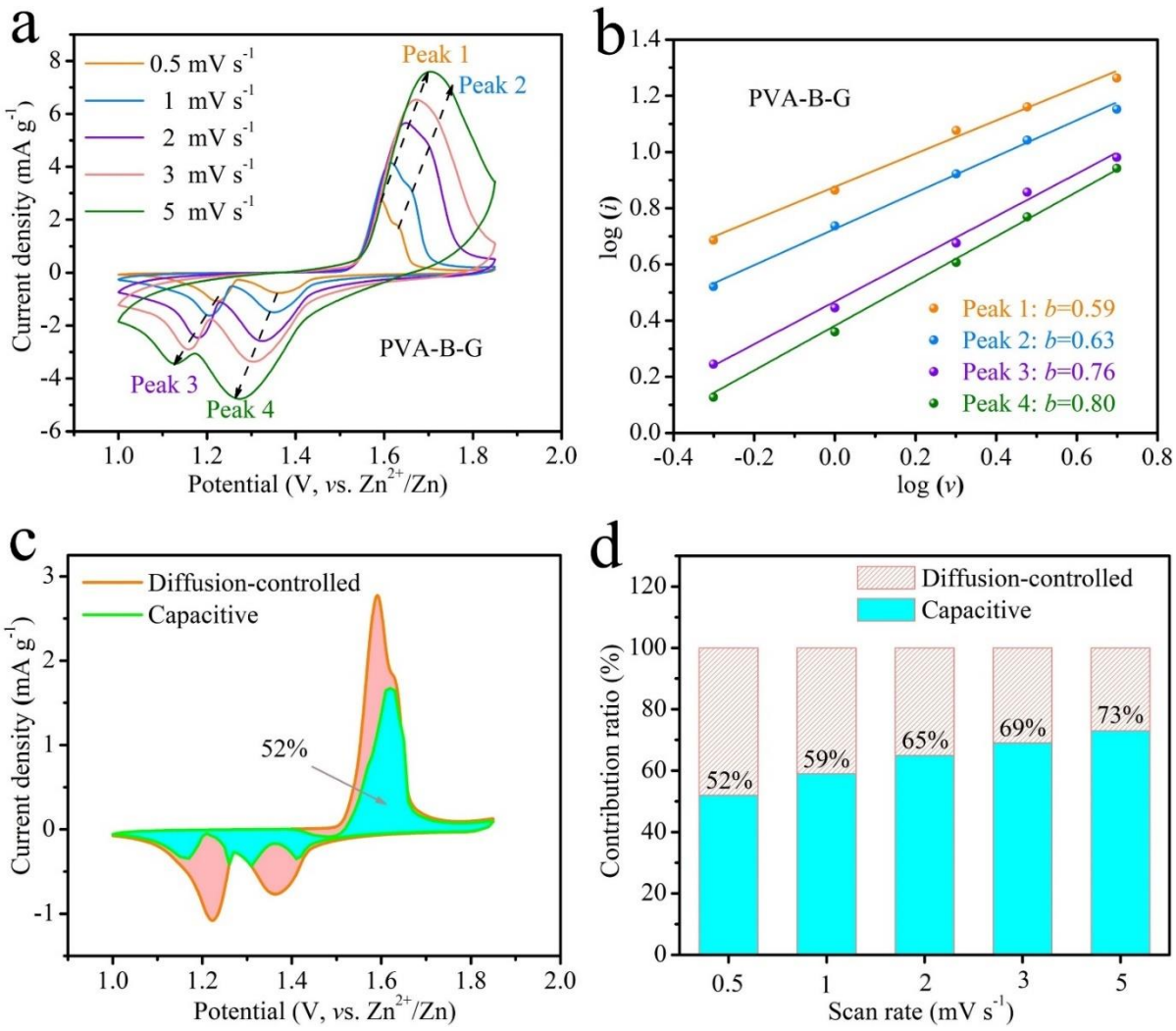

Fig. S12 (a) CV curves at scan rates from 0.5 to 5 mV s^{-1} (25 °C), (b) the linear fit between log (*i*) and log (*v*) of four redox peaks, (c) the capacity contribution analysis at 0.5 mV s^{-1}, and (d) contribution ratios of diffusion controlled and capacitive capacities at different scan rates of PVA-B-G battery.

To achieve a better understanding of electrochemical kinetics of PVA-B-G battery, CV measurements were carried out at various scan rates at 25 °C (Fig. S12a). As the scan rate increases, the anodic peaks move to the positive direction, while the cathodic peaks shift to the opposite direction at the same time. Meanwhile, these peaks become broader with the increase of scan rate. This phenomenon is due to increased polarization at higher scan rates. If assuming that the peak current (*i*) obeys a power-law relationship with the scan rate (*v*), the general relationship between them can be described using the following equation:[17]

$$i = av^b \quad (2)$$

A higher *b* value would reflect higher contribution from capacitive charge storage, *i.e.*, more favored electrochemical kinetics. Based on the linear fitting between log (*i*) and log (*v*) (Fig. S12b), the *b* values associated with four redox peaks are calculated to be 0.59, 0.63, 0.76, and 0.80, meaning that the capacitive behavior occupies a large portion. Furthermore, the capacitive contribution is separated using the following equation:[18-21]

$$i(V) = k_1 v + k_2 v^{1/2} \qquad (3)$$

where $k_1 v$ and $k_2 v^{1/2}$ stand for the capacitive and diffusion-controlled parts of the current response ($i(V)$), respectively. In Fig. S12c, the capacitive contribution is highlighted by the cyan color, suggesting that the capacitive charge storage in the PVA-B-G battery occurs to a large extent. The diffusion-controlled and capacitive contributions to the capacity of PVA-B-G battery are displayed in Fig. S12d. As the scan rate rises from 0.5 to 5 mV s^{-1}, the capacitive contribution ratio grows from 52% to 73%. That is, the capacitive charge storage accounts for more than half of the total capacity, and its proportion goes up with the scan rate.

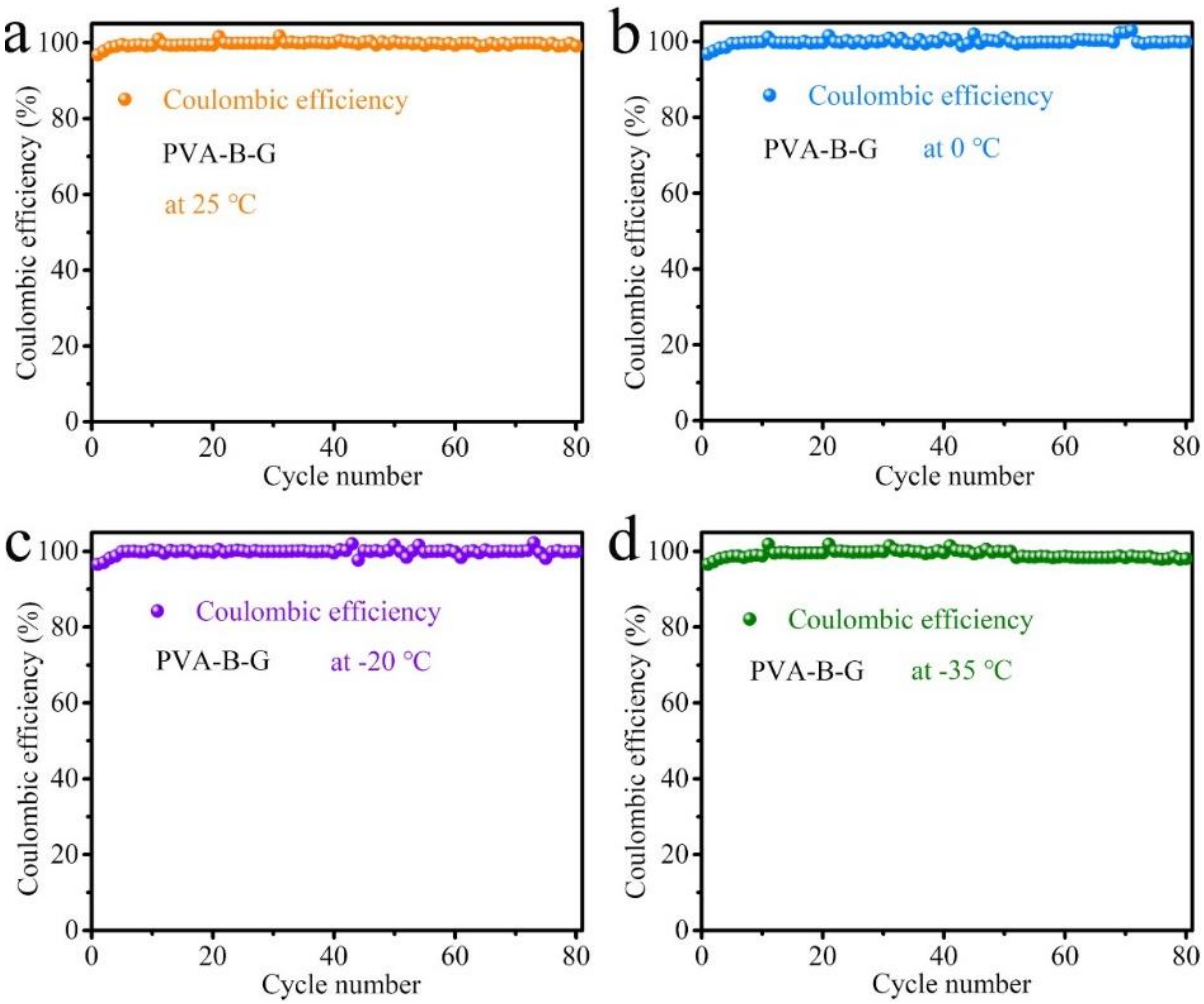

Fig. S13 The coulombic efficiency of PVA-B-G battery as a function of the cycle number during the rate-performance tests in Fig. 4a−d: (a) at 25 ºC, (b) at 0 ºC, (c) at −20 ºC, and (d) at −35 ºC.

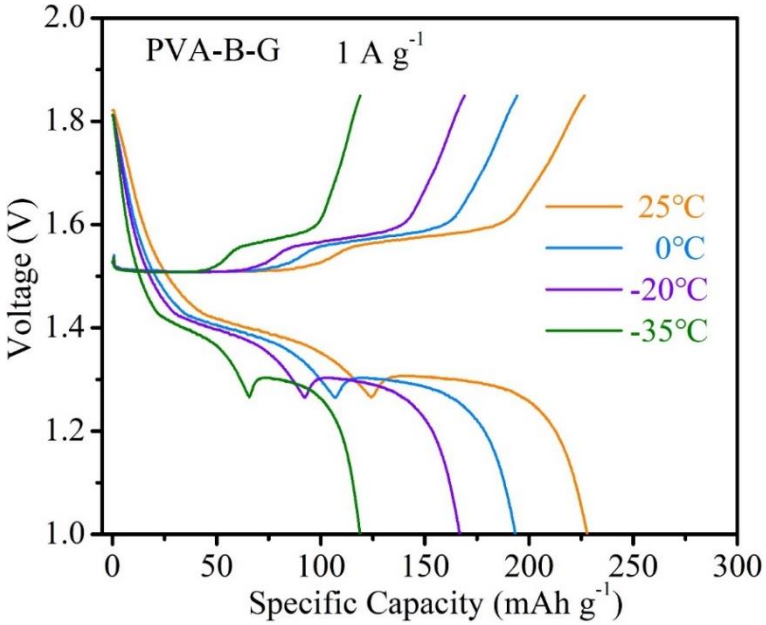

Fig. S14 GCD curves of the PVA-B-G battery at 1 A g^{-1} at different temperatures.

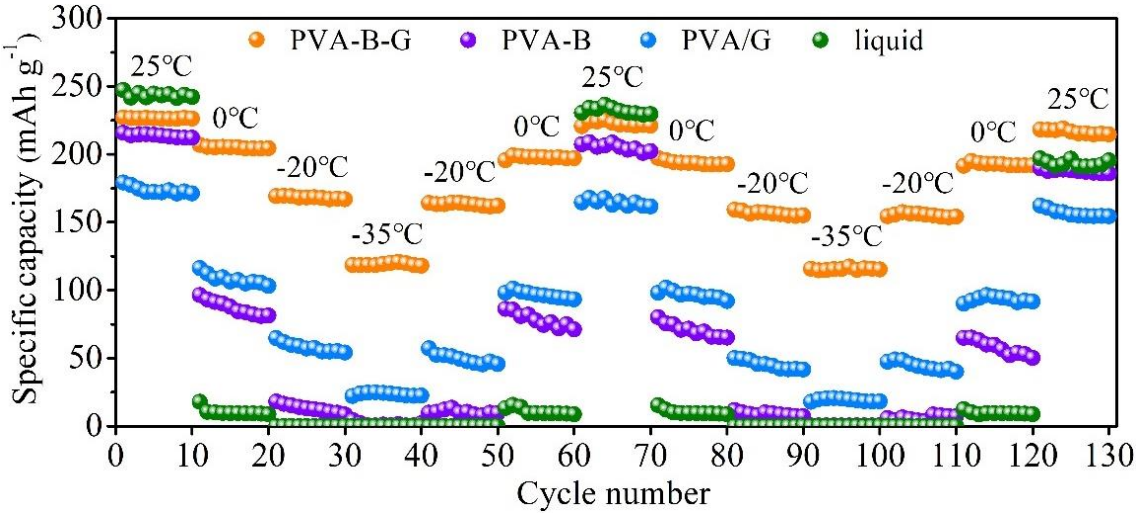

Fig. S15 Cycling performances at 1 A g^{-1} of four types of batteries when undergoing different working temperatures in succession.

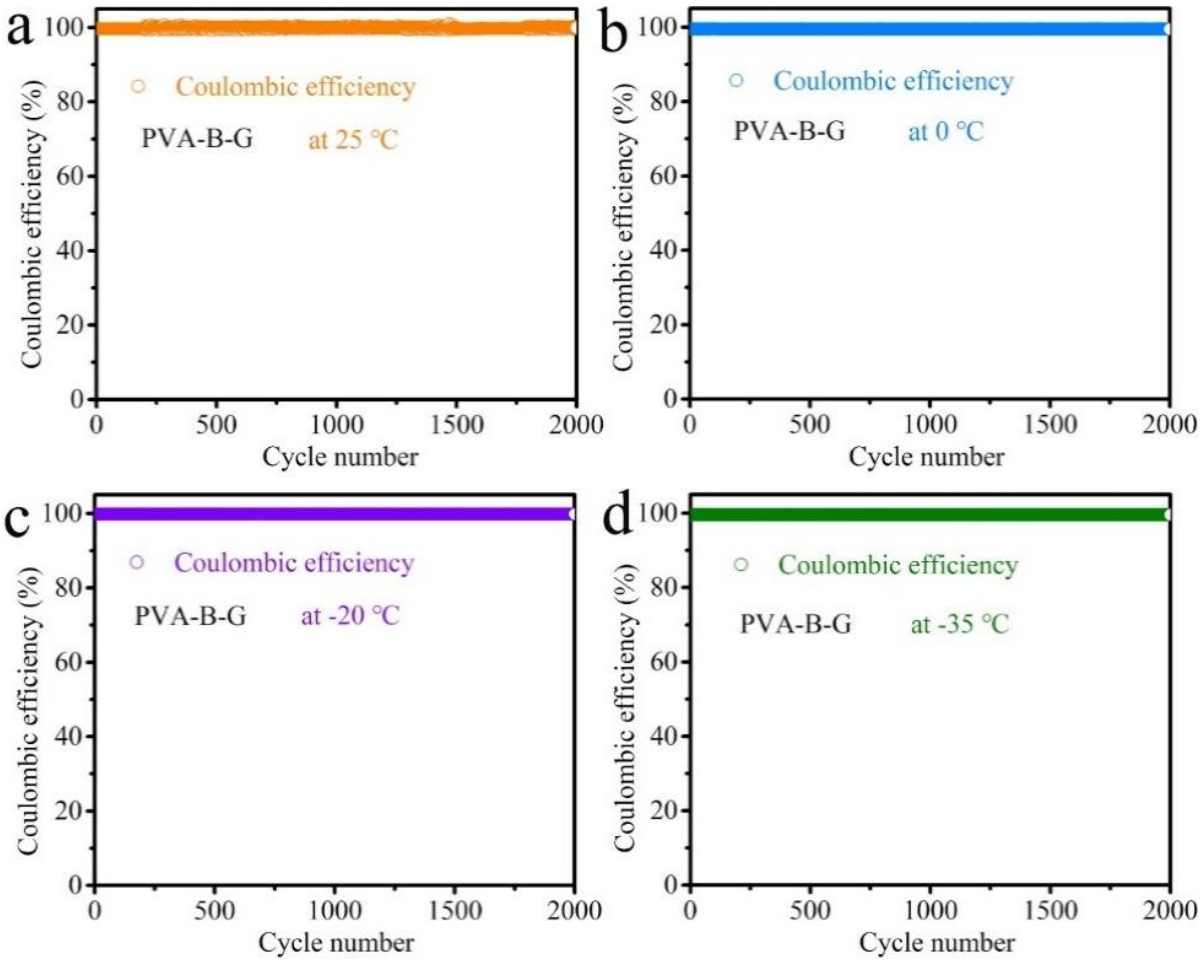

Fig. S16 The coulombic efficiency of PVA-B-G battery as a function of the cycle number during the cycling-performance tests in Fig. 5a: (a) at 25 ºC, (b) at 0 ºC, (c) at −20 ºC, and (d) at −35 ºC.

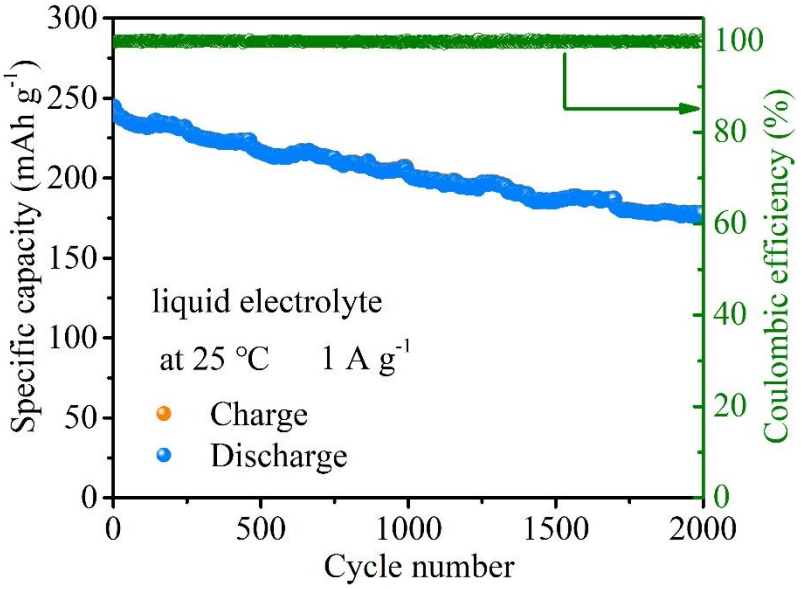

Fig. S17 Cycling performance of the liquid-electrolyte battery at 1 A g^{-1} at 25 °C.

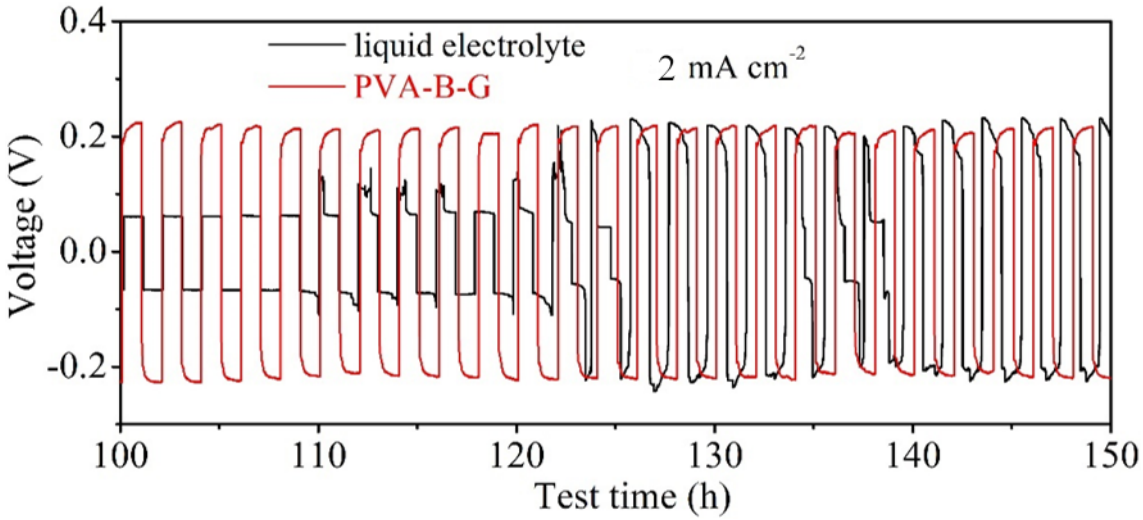

Fig. S18 GCD voltage profiles of Zn//Zn symmetrical cells with PVA-B-G and liquid electrolytes cycled at 2 mA cm^{-2} during the 100^{th}–150^{th} h testing period.

Supplementary videos

Video S1 Demonstration of four PVA-B-G batteries connected in series to charge a mobile phone.

Video S2 Demonstration of a PVA-B-G battery powering an electric timer when it is hammered.

References

1. J. Z. Chen, J. L. Xu, S. Zhou, N. Zhao and C. P. Wong, *Nano Energy*, 2015, **15**, 719-728.
2. F. N. Mo, G. J. Liang, Q. Q. Meng, Z. X. Liu, H. F. Li, J. Fan and C. Y. Zhi, *Energy Environ. Sci.*, 2019, **12**, 706-715.
3. S. L. Zhang, N. S. Yu, S. Zeng, S. S. Zhou, M. H. Chen, J. T. Di and Q. W. Li, *J. Mater. Chem. A*, 2018, **6**, 12237-12243.
4. X. Li, L. Ma, Y. Zhao, Q. Yang, D. Wang, Z. Huang, G. Liang, F. Mo, Z. Liu and C. Zhi, *Mater. Today Energy*, 2019, **14,** 100361.
5. Q. Yang, F. Mo, Z. Liu, L. Ma, X. Li, D. Fang, S. Chen, S. Zhang and C. Zhi, *Adv. Mater.*, 2019, **31**, 1901521.
6. S. Huang, F. Wan, S. S. Bi, J. C. Zhu, Z. Q. Niu and J. Chen, *Angew. Chem. Int. Edit.*, 2019, **58**, 4313-4317.
7. H. F. Li, Z. X. Liu, G. J. Liang, Y. Huang, Y. Huan, M. S. Zhu, Z. X. Pei, Q. Xue, Z. J. Tang, Y. K. Wang, B. H. Li and C. Y. Zhi, *ACS Nano*, 2018, **12**, 3140-3148.
8. Q. Li, X. Cui and Q. Pan, *ACS Appl. Mater. Interf.*, 2019, **11**, 38762-38770.
9. H. F. Li, C. P. Han, Y. Huang, Y. Huang, M. S. Zhu, Z. X. Pei, Q. Xue, Z. F. Wang, Z. X. Liu, Z. J. Tang, Y. K. Wang, F. Y. Kang, B. H. Li and C. Y. Zhi, *Energy Environ. Sci.*, 2018, **11**, 941-951.
10. H. Li, Q. Yang, F. Mo, G. Liang, Z. Liu, Z. Tang, L. Ma, J. Liu, Z. Shi and C. Zhi, *Energy Storage Mater.*, 2019, **19**, 94-101.
11. D. Wang, H. Li, Z. Liu, Z. Tang, G. Liang, F. Mo, Q. Yang, L. Ma and C. Zhi, *Small*, 2018, **14**, 1803978.
12. L. Ma, N. Li, C. Long, B. Dong, D. Fang, Z. Liu, Y. Zhao, X. Li, J. Fan, S. Chen, S. Zhang and C. Zhi, *Adv. Funct. Mater.*, 2019, **29**, 1906142.
13. X. Zhang, Z. Pei, C. Wang, Z. Yuan, L. Wei, Y. Pan, A. Mahmood, Q. Shao and Y. Chen, *Small*, 2019, **15**, 1903817.
14. Q. Han, X. Chi, S. Zhang, Y. Liu, B. Zhou, J. Yang and Y. Liu, *J. Mater. Chem. A*, 2018, **6**, 23046-23054.
15. Y. Huang, J. Zhang, J. Liu, Z. Li, S. Jin, Z. Li, S. Zhang and H. Zhou, *Mater. Today Energy*, 2019, **14**, 100349.
16. J. Zhao, K. K. Sonigara, J. Li, J. Zhang, B. Chen, J. Zhang, S. S. Soni, X. Zhou, G. Cui and L. Chen, *Angew. Chem.*, 2017, **129**, 7979-7983.
17. V. Augustyn, J. Come, M. A. Lowe, J. W. Kim, P. L. Taberna, S. H. Tolbert, H. D. Abruna, P. Simon and B. Dunn, *Nat. Mater.*, 2013, **12**, 518-522.
18. L. N. Chen, Y. S. Ruan, G. B. Zhang, Q. L. Wei, Y. L. Jiang, T. F. Xiong, P. He, W. Yang, M. Y. Yan, Q. Y. An and L. Q. Mai, *Chem. Mater.*, 2019, **31**, 699-706.
19. F. W. Ming, H. F. Liang, Y. J. Lei, S. Kandambeth, M. Eddaoudi and H. N. Alshareef, *ACS Energy Lett.*, 2018, **3**, 2602-2609.
20. B. Y. Tang, G. Z. Fang, J. Zhou, L. B. Wang, Y. P. Lei, C. Wang, T. Q. Lin, Y. Tang and S. Q. Liang, *Nano Energy*, 2018, **51**, 579-587.
21. H.-S. Kim, J. B. Cook, H. Lin, Jesse S. Ko, Sarah H. Tolbert, V. Ozolins and B. Dunn, *Nat. Mater.*, 2016, **16**, 454.